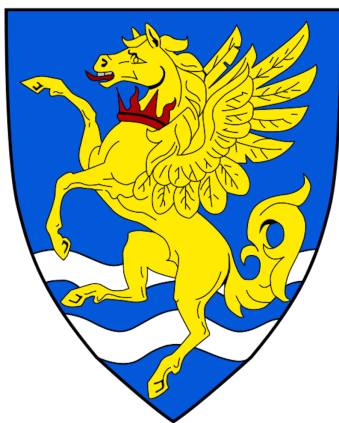


APPROACHING THE MARANGONI EFFECT
THROUGH
EQUILIBRIUM MOLECULAR DYNAMICS

H. G. A. BURTON
ROBINSON COLLEGE
CAMBRIDGE



Declaration

This dissertation is submitted in partial fulfilment of the requirements for Part III Chemistry. It describes work carried out in the Department of Chemistry in the Michaelmas Term 2015 and the Lent Term 2016. Unless otherwise indicated, the research described is my own and not the product of collaboration.

Acknowledgements

Acknowledgements will go here.

APPROACHING THE MARANGONI EFFECT THROUGH EQUILIBRIUM MOLECULAR DYNAMICS

H. G. A. BURTON

Abstract

The Marangoni flow induced by a temperature gradient at a liquid–liquid interface is studied through the use of equilibrium molecular–dynamics simulations for a symmetric Lennard–Jones binary–mixture. An artificial Marangoni force is computed by considering the finite difference in the transverse component of the stress–tensor for two equilibrium simulations at different temperatures. Applying this as a body force to an equilibrium simulation at an intermediate temperature allows the Marangoni flow profile to be computed. This is demonstrated for a binary–mixture confined within a piston and a binary–mixture periodic in all dimensions. Because the atomic stress–tensor is not uniquely defined, the use of the Virial and Irving–Kirkwood stress–tensor is compared. Finally, the method is used to observe the retardation of Marangoni flows due to the addition of surfactant molecules.

Contents

Declaration	i
Acknowledgements	i
Abstract	ii
1 Introduction	1
1.1 Experimental studies	2
1.2 Striving for a microscopic description	2
2 Theoretical Background	4
2.1 The macroscopic description	4
2.2 A microscopic approach	5
2.3 The Finite Difference Approach	6
2.4 Non-uniqueness of the pressure tensor	6
3 Computational Methods	9
3.1 Interaction Model	9
3.2 Reduced Units	10
3.3 Thermostats	10
3.4 Barostats	11
3.5 Preparing the system	11
3.6 Calculating the stress tensor	12
3.7 Computing averages	12
3.8 Modelling surfactant molecules	13
3.9 Software details	14
4 Results and Discussion	15
4.1 Binary-mixture confined between two walls	15
4.1.1 Using the Virial stress	15
4.1.2 Comparing to the Irving-Kirkwood stress	18
4.2 Binary-mixture periodic in 3-dimensions	21
4.2.1 Comparing the Virial and Irving-Kirkwood stress	22
4.2.2 Reducing the noise in the force-profile	25
4.3 The effect of surfactants	28

5	Concluding Remarks	33
5.1	Future directions of study	34
	Bibliography	36

1 Introduction

Interfacial flows resulting from a chemical potential or temperature gradient were first reported by J. Thompson in 1855.¹ After forming the basis of Carlo Marangoni's doctoral dissertation in 1865, this phenomenon was termed the "Marangoni Effect".² Since then, temperature induced Marangoni flows, also known as thermocapillary motion, have been the focus of a number of scientific studies.

Through the works of Derjaguin et al.³ and Levich⁴, a thorough macroscopic description has been developed. Anderson summarises these results in the context of phoresis.⁵

On the simplest level, the effect is described as a result of an interfacial tension gradient. Experimental studies show that hot fluids have a lower surface tension than cold fluids,^{6,7} and thus motion occurs in the opposite direction to an applied temperature gradient. However, this analysis does not progress far since the temperature dependence of surface tension is not rigorously understood.

Regardless, Levich used hydrodynamics to derive the fluid velocity across a shallow pan in terms of $\partial\gamma/\partial T$.⁴ He achieved this result using a continuity equation setting the total flow to zero. This implied that any interfacial flows are accompanied by an opposing flow in the bulk fluid.

In contrast, Derjaguin et al. calculated the momentum flux from an applied temperature gradient by computing the energy flux carried by a pressure-driven convection and applying Onsager's reciprocal rule.³ They showed that this velocity can be related to the excess enthalpy density near the interface (compared to the bulk fluid), yielding a macroscopic description.

However, these theories are founded upon a thermodynamic backbone which relies on knowledge of the macroscopic system. Marangoni flows are inherently a microscopic phenomenon, localised at fluid interfaces, and thus a thermodynamic description cannot faithfully describe this effect. Instead, a microscopic theory based on interparticle interactions is required. No such theory currently exists, and there has been limited research in this area.⁸

By studying the microscopic properties of a liquid-liquid interface, this report aims to model the Marangoni effect and investigate the link between the microscopic fluid properties and its macroscopic motion.

1.1 Experimental studies

Despite the lack of a microscopic theory, there has been substantial experimental research into the Marangoni effect. Many of these studies have focussed on the more curious examples of Marangoni flows, such as Thompson’s “tears of wine”^{1,9–11} and the “coffee ring effect”,^{12–14} whilst others have shown its importance in technological applications. For example, Sternling and Scriven¹⁵ proposed Marangoni effects as the origin of interfacial turbulence and mass transport, yielding applications in fluid mixing and oil recovery.^{16–18} Furthermore, Subramanian and Balasubramanian outlined the importance of Marangoni forces for the motion of bubbles and droplets in reduced gravity.¹⁹

In 1959, Young et al. produced a theoretical description of this motion of bubbles and droplets under the influence of a temperature gradient, a phenomenon termed thermophoresis.²⁰ They described how this gradient causes a higher surface tension on the low temperature side of the droplet, resulting in a force pulling the surrounding fluid towards this region. A corresponding reaction force then propels the droplet towards the warmer fluid. Analogously to electrophoresis, there is no net force acting on the fluid within the droplet.

This force was measured experimentally by S. C. Hardy,²¹ who used a temperature gradient to balance the Marangoni and buoyancy forces acting on a droplet within a fluid, thus holding the droplet stationary. Later theoretical modelling by Kim and Subramanian suggested that the inclusion of surface-active substances could be used to prevent thermophoresis,^{22,23} a prediction that was confirmed experimentally.^{24,25}

With the advances in space technology, thermophoresis and thermocapillary motion have become important mechanisms for fluid motion and mass transfer in low-gravity environments, where surface effects dominate over buoyancy driven motion. The motion of bubbles and drops due to interfacial gradients is considered key for materials processing in space, enabling phase separation of binary mixtures and the potential to make uniform composite materials.²⁴ Moreover, fluid transport in the absence of gravity is important for controlling fluids aboard satellites.

1.2 Striving for a microscopic description

With many potential applications, the search for a microscopic description is becoming ever more significant, and computer simulations are increasingly being used

to understand this phenomenon. Marangoni flows are inherently dynamic and can therefore be studied using a time-dependent method such as molecular dynamics. Modelling the behaviour of a partially miscible binary-mixture under the effect of a temperature gradient might initially appear trivial; simply create a temperature gradient in a system and measure the subsequent particle velocities. This non-equilibrium approach was used by Hampe et al. in their study of the Marangoni effect.⁸ Despite their positive results, the method is complicated by the use of periodic boundary conditions that require each unit cell to have two temperature gradients, such that the temperature gradient is also periodic. Any flow due to this gradient then generates an opposing concentration gradient, and an equilibrium state will be reached.

In the present study, I investigate the use of equilibrium molecular dynamics simulations for modelling the Marangoni effect. By calculating the equilibrium stress acting on a binary-mixture for two different temperatures, the derivative of the transverse stress with respect to temperature can be estimated and used to compute a body force. This can then be applied in an equilibrium simulation at an intermediate temperature to imitate the Marangoni force, thus circumventing the complications of a periodic temperature profile. By measuring the velocity profile in this final simulation, Marangoni flows can be observed.

Using this equilibrium method, I show that a Marangoni force at a liquid-liquid interface can be calculated from the transverse stress tensor and used to generate a Marangoni flow. The effect of surfactants on the magnitude of the Marangoni flow is then investigated and compared to experimental observations.

The theoretical description of the Marangoni effect is described in Section 2, whilst Section 3 outlines the computational methods used. The simulation results are discussed in Section 4. Section 5 provides a summary of the conclusions and proposes directions for future studies.

2 Theoretical Background

2.1 The macroscopic description

The motion of fluids may be described macroscopically using the Navier–Stokes equation.²⁶ This models liquids as a continuous medium and combines the conservation of mass and momentum with the relation between the force on a volume element and the local fluid flow. In the low Reynolds-number regime the flow velocity is small, and the Navier–Stokes equation reduces to

$$\eta \nabla^2 \mathbf{v}(r, t) = \nabla P(r, t) - \mathbf{f}(r). \quad (1)$$

Equation 1 shows that motion in fluids *can only* occur under the presence of a pressure gradient or external forces. In the case of Marangoni flows, motion due to the temperature gradient must result from induced local pressure gradients, which may be derived from thermodynamics.

Consider a binary–mixture with an interface at $z = 0$. The Gibbs–Duhem equation gives

$$V dP = \sum_{i=0}^n N_i d\mu_i + S dT. \quad (2)$$

The bulk fluid pressure is constant and isotropic, giving

$$\left(\frac{\partial P}{\partial x} \right) = \sum_{i=0}^n \rho_i^B \left(\frac{\partial \mu_i}{\partial x} \right) + \frac{S}{V} \left(\frac{\partial T}{\partial x} \right) = 0. \quad (3)$$

The Maxwell relations relate the entropy to the partial differential of chemical potential with respect to temperature through

$$\left(\frac{\partial \mu_i}{\partial T} \right)_{P, N_i} = - \left(\frac{\partial S}{\partial N_i} \right)_{P, T}. \quad (4)$$

The total entropy is the weighted sum of the partial entropy of the species in the system,

$$S = \sum_{i=0}^n s_i N_i, \quad (5)$$

thus

$$\left(\frac{\partial \mu_i}{\partial T} \right)_{P, N_i} = -s_i. \quad (6)$$

This allows Equation 3 to be expressed as

$$\left(-\sum_{i=1}^n \rho_i^{\text{B}} s_i^{\text{B}} + \frac{S^{\text{B}}}{V} \right) \left(\frac{\partial T}{\partial x} \right) = 0, \quad (7)$$

for which the solution is

$$\frac{S^{\text{B}}}{V} = \sum_{i=1}^n \rho_i^{\text{B}} s_i^{\text{B}}. \quad (8)$$

Consider the case close to an interface or surface where the pressure will deviate from its bulk value. Since μ_i and T are independent of z ,

$$\left(\frac{\partial \mu_i}{\partial T} \right) = -s_i^{\text{B}}, \quad (9)$$

and the pressure gradient reduces to

$$\left(\frac{\partial P(z, x)}{\partial x} \right) = \left(\sum_{i=1}^n \rho_i(z) \left(s_i(z) - s_i^{\text{B}} \right) \right) \left(\frac{\partial T}{\partial x} \right). \quad (10)$$

For an ideal mixture, the partial entropy is given by $s_i = \frac{1}{T} (\mu_i - h_i)$, and thus Equation 10 can be expressed in terms of the excess enthalpy density, $\Delta h(z)$,

$$\left(\frac{\partial P(z, x)}{\partial x} \right) = -\Delta h(z) \frac{1}{T} \left(\frac{\partial T}{\partial x} \right) = -\Delta h(z) \left(\frac{\partial \ln T}{\partial x} \right). \quad (11)$$

Substituting Equation 11 into Equation 1 and assuming there is no pressure gradient in the z or y direction allows the velocity, $v(z)$, at the interface to be computed as

$$v(z=0) = -\frac{1}{\eta} \int_0^\infty dz z \Delta h(z) \frac{\partial T}{\partial x} \quad (12)$$

where it has been assumed that the fluid in the bulk is at rest ($v_x(z=\infty) = 0$). This expression is almost equivalent to that derived by Derjaguin et al., except for a factor of two, suggesting a potential error in Derjaguin's approach.^{3,5}

2.2 A microscopic approach

The Marangoni effect is a phenomenon occurring on microscopic length-scales, and hence a macroscopic hydrodynamic approach is not entirely appropriate. Instead of

solving the Navier–Stokes equation, the velocity should be related directly to the local forces acting on the fluid, which may be calculated from the local stress tensor,

$$f_x(z) = - \left(\frac{\partial \sigma_{xx}(z, x)}{\partial x} \right). \quad (13)$$

In the case of Marangoni flows, the force is due to a temperature gradient and $f_x(z)$ can be calculated from the chain rule as

$$f_x(z) = - \left(\frac{\partial \sigma_{xx}(z, x)}{\partial T} \right) \left(\frac{\partial T}{\partial x} \right). \quad (14)$$

2.3 The Finite Difference Approach

Equation 14 shows that the force due to a temperature gradient can be inferred from the temperature variation of the stress tensor. To a first order approximation, the temperature gradient of the stress tensor can be calculated using a finite difference approach as

$$\left(\frac{\partial \sigma_{xx}(z, x)}{\partial T} \right) \approx \frac{\sigma_{xx}^{T_2}(z, x) - \sigma_{xx}^{T_1}(z, x)}{T_2 - T_1}. \quad (15)$$

Using this approximation, the Marangoni flow profile can be computed as follows:

1. Compute $\sigma_{xx}(z)$ for an equilibrium system at a given temperature T_1 .
2. Repeat the calculation for another equilibrium system at a slightly higher temperature T_2 .
3. Approximate the partial derivative of the transverse stress with respect to temperature using the finite difference, Equation 15.
4. Infer $f_x(z)$ for a specified value of $\partial T / \partial x$ using Equation 14 to calculate a force profile.
5. Compute the flow profile by applying $f_x(z)$ as an artificial body force to an equilibrium simulation at an intermediate temperature T_3 (where $T_1 < T_3 < T_2$).

2.4 Non-uniqueness of the pressure tensor

The stress tensor is intimately related to the pressure tensor through

$$\sigma_{\alpha\beta}(\mathbf{r}) = -P_{\alpha\beta}(\mathbf{r}). \quad (16)$$

The pressure tensor is composed of a kinetic contribution, arising from the momentum transfer of particles on the container walls, and a potential contribution attributed to the interparticle forces.²⁷ The kinetic part may be calculated from the ideal gas contribution,

$$\mathbf{P}^K(\mathbf{r}) = k_B T \rho(\mathbf{r}) \hat{\mathbf{I}}, \quad (17)$$

whilst the potential contribution cannot be uniquely defined.

For a homogeneous fluid the stress tensor is isotropic, with each diagonal element equal to $-P$, where P is the bulk hydrostatic pressure. This pressure can be calculated using the Virial equation, originally derived from the Virial theorem of Clausius²⁸, (although also derivable by differentiating the canonical partition function²⁹) to give

$$P_{\alpha\beta}(\mathbf{r}) = \frac{1}{V} \left(-m(\mathbf{r}) \langle \nu_\alpha \nu_\beta \rangle + \frac{1}{2} \sum_i^N \sum_{j \neq i}^N (r_\alpha^{(i)} - r_\alpha^{(j)}) f_\beta^{ij} \right). \quad (18)$$

Clausius' formulation calculates the local pressure by considering the forces acting on particles located within a volume element at \mathbf{r} .

In an inhomogeneous system there is an ambiguity over which particles should contribute to the force at a given position.^{27,29,30} This was first reported by Irving and Kirkwood^{31,32} who described an alternative method that computes the pressure tensor from the forces acting across an infinitesimal surface $d\mathbf{A}$ located at \mathbf{r} . They calculate the local pressure tensor using only pairs of particles for which the line connecting their centers of mass passes through $d\mathbf{A}$. For planar systems, such as those involving an interface in the (x, y) plane, the pressure tensor depends only on the distance from this interface and the normal and tangential components can be expressed as

$$P_N^{\text{IK}}(z) = \rho(z) k_B T - \frac{1}{2A} \left\langle \sum_{i \neq j} \frac{|z_{ij}|}{r_{ij}} U'(r_{ij}) \Theta \left(\frac{z - z_i}{z_{ij}} \right) \Theta \left(\frac{z_j - z}{z_{ij}} \right) \right\rangle, \quad (19)$$

$$P_T^{\text{IK}}(z) = \rho(z) k_B T - \frac{1}{4A} \left\langle \sum_{i \neq j} \frac{x_{ij}^2 + y_{ij}^2}{r_{ij}} \frac{U'(r_{ij})}{|z_{ij}|} \Theta \left(\frac{z - z_i}{z_{ij}} \right) \Theta \left(\frac{z_j - z}{z_{ij}} \right) \right\rangle. \quad (20)$$

The Irving–Kirkwood stress has advantages over the Virial method for studying confined systems. In particular it yields a normal component independent of local fluctuations in the number density. Density fluctuations occur close to walls due to structural layering of the fluid, and there is reduced density at liquid–liquid

interfaces from the finite width of the interfacial region. As a result, oscillations in the normal component of the Virial pressure are observed in such systems²⁷ whilst the Irving–Kirkwood pressure yields a constant normal component, equal to the bulk hydrostatic pressure. This is more consistent with the expected result since the fluid is isotropic in the direction normal to the surface.

3 Computational Methods

Equilibrium molecular dynamics simulations of a symmetric binary-mixture of partially miscible fluids were used to measure the stresses acting on the fluid at two different temperatures. The Marangoni force was then inferred using Equation 15. Where possible, this force was applied as an artificial body force in a simulation at an intermediate temperature to generate a Marangoni flow profile.

Two key systems were studied, a symmetric binary-mixture under three-dimensional periodic boundary conditions, and a binary-mixture periodic in the (x, y) plane but confined between two walls in the z -dimension, as shown in Figure 1. All molecular dynamics simulations were executed using the LAMMPS (Large Atomic and Molecular Massively Parallel Simulator) package.³³

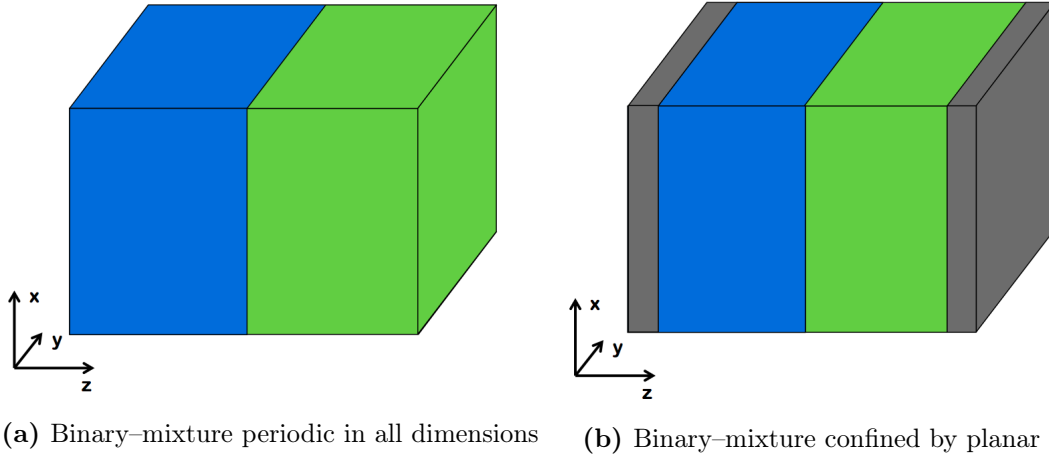


Figure 1: Both the systems studied incorporated a partially miscible binary-mixture of Fluid A (blue) and Fluid B (green). For the mixture periodic in all dimensions, the pressure is regulated using a Nosé-Hoover barostat. In the confined fluid, the walls are used to create a piston and an external force equal to $P_{\text{ext}} \times A_{\text{wall}}$ is applied.

3.1 Interaction Model

The fluids were modelled using spherical particles and their interaction was tuned to a pair-wise truncated Lennard-Jones potential:

$$V(\mathbf{r}^N) = \frac{1}{2} \sum_{i \neq j} \phi(r_{ij}) \quad (21)$$

where

$$\phi(r_{ij}) = 4\epsilon_{ij} \left(\left(\frac{\sigma_{ij}}{r_{ij}} \right)^{12} - \left(\frac{\sigma_{ij}}{r_{ij}} \right)^6 \right) \text{ for } r \leq r_c \quad (22)$$

$$\phi(r_{ij}) = 0 \text{ for } r > r_c. \quad (23)$$

This potential involves an attractive r_{ij}^{-6} term accounting for the long-range Van der Waal's interaction and a short-range r_{ij}^{-12} repulsive term corresponding to the Pauli repulsion between particles. The length-scale of the potential is given by σ_{ij} (chosen to be equal for all pairs of i and j) while the parameter ϵ_{ij} determines the strength of the interaction.

The miscibility of the two fluids (A and B) can be controlled using the relative values of the interaction parameter; in this study the values chosen were:

$$\epsilon_{A,A} = \epsilon_{B,B} = 1.0, \quad (24)$$

$$\epsilon_{A,B} = 0.55, \quad (25)$$

in agreement with previous studies on similar Lennard-Jones binary-mixtures.^{8,34,35} The cutoff for the potential was chosen to be $r_c = 4 \sigma$.

3.2 Reduced Units

Physical quantities including distances and energies are expressed in terms of reduced units. For a Lennard-Jones system, the basic units are σ for length, ϵ for energy and m for mass, from which all other units may be derived.³⁶ Physical quantities become dimensionless when expressed in terms of these units, for example $r^* \equiv r/\sigma$. Scaled coordinates expressed relative to the simulation box size are also used, for example $z' = z^*/L_{z^*}$ where L_{z^*} is the dimension of the box in the z -direction. These are useful if the box-dimensions vary, such as when a barostat acts on the system.

3.3 Thermostats

In molecular dynamics simulations, the temperature is controlled using thermostats, which simulate the coupling of the system to an external heat bath.

Thermostats work by applying a stochastic frictional force to particles, either by adding a random force to momenta (Langevin)³⁷ or reassigning the velocity of randomly chosen particles to that obtained from the Maxwell distribution (Anderson)³⁸.

The Nosé–Hoover thermostat was used throughout this study. This introduces a fictitious frictional force into the equations of motion, adjusting the particle velocities until the temperature is equal to the desired value.^{39–41} The equations of motion in three–dimensions become:

$$m_i \frac{d^2 \mathbf{r}}{dt^2} = \mathbf{f}_i - \zeta m_i \mathbf{v}_i \quad (26)$$

$$\frac{d\zeta(t)}{dt} = \frac{1}{Q} \left[\sum_{i=1}^N m_i \frac{\mathbf{v}_i^2}{2} - \frac{3N+1}{2} k_B T \right]. \quad (27)$$

The result is a system where the energy fluctuates but the combined energy of the system and heat bath remains constant, maintaining a canonical ensemble.

3.4 Barostats

The bulk pressure of the fluid must also be held constant. A piston provides the simplest method and is relatively easy to create; the fluid is confined between two solid walls and a force equal to $P_{ext} \times A_{wall}$ is applied. This was used for studying the binary–mixture confined between two walls. In the case of Marangoni flows, a thermocapillary effect will also occur at the boundary of the liquid and the solid piston. The interface must be sufficiently far from the walls such that this thermocapillary force can be ignored. Only the interfacial force should then be applied in the final simulation.

Alternatively a Nosé–Hoover barostat can regulate the pressure by adjusting the simulation box dimensions and altering the equations of motion accordingly.^{39–41} When studying surface effects, the box size must only be changed in the direction perpendicular to the interface, since any other direction will alter its area and create an error in the thermodynamic pressure,

$$P = - \left(\frac{\partial F}{\partial V} \right)_T + \gamma \left(\frac{\partial A}{\partial V} \right)_T. \quad (28)$$

3.5 Preparing the system

The fluid was prepared from a face–centred cubic lattice with a spacing of 1.64414σ and a simulation box size of $L_x^* = 13.1531$, $L_y^* = 13.1531$ and $L_z^* = 32.8828$. This lattice was melted over 2×10^6 timesteps of length 0.001τ to generate a fluid state. The barostat was set to a pressure of $P^* = 0.1$ and the temperatures used were $T^* = 0.8$ and $T^* = 0.9$, ensuring the system occupied the liquid region of

the Lennard–Jones phase space.⁴² Solid walls in the system were constructed with a harmonically bonded lattice using a spring constant of $K^* = 2500$ and an equilibrium bond length of $r_0^* = 1.163$.

3.6 Calculating the stress tensor

The Virial stress tensor was calculated using an in-built function within the LAMMPS package, which returns the stress tensor for each atom. However, LAMMPS does not have a method for calculating the Irving–Kirkwood stress tensor. Instead this was calculated by saving the particle positions on a given timestep to a file and post-processing. The stress tensor was then computed using a programme written by R. Ganti and adapted for the specific systems studied. Since the Virial method is implemented in parallel whilst the Irving–Kirkwood method is not, the Irving–Kirkwood stress was significantly more expensive to compute, incurring approximately a 4-fold increase in computational time.

3.7 Computing averages

Usually time-averages of physical observables are calculated in molecular dynamics simulations. In the systems studied, the observables are the number density, stress tensor and particle velocities. Their values were measured on every timestep and spatially averaged into 400 planar slabs across the z -dimension of the box. These spatial averages were then time-averaged over the full duration of the simulation.

Under the ergodic hypothesis, time-averages can be equated to ensemble averages for an infinitely long simulation time.⁴³ Practically, however, these averages must be evaluated over a finite time period, and have an associated statistical error. The method of block-averaging, developed by Flyvbjerg and Peterson, provides an efficient technique for computing this error.⁴⁴ They show that the variance of an observable, A , can be estimated by

$$\text{var}(A) \geq \left\langle \frac{C_0}{n-1} \right\rangle, \quad (29)$$

where C_0 is the value of the time-correlation function for the block-transformed data at $t = 0$ and is given by

$$C_0 \equiv \frac{1}{n} \sum_{k=1}^n (A_k - \bar{A}) (A_k - \bar{A}). \quad (30)$$

A lower bound for the variance can be calculated by finding the block length at which this estimate reaches a plateau. Furthermore, the error in the variance can be estimated as

$$\sqrt{\frac{2}{n-1} \times \frac{C_0}{n-1}}. \quad (31)$$

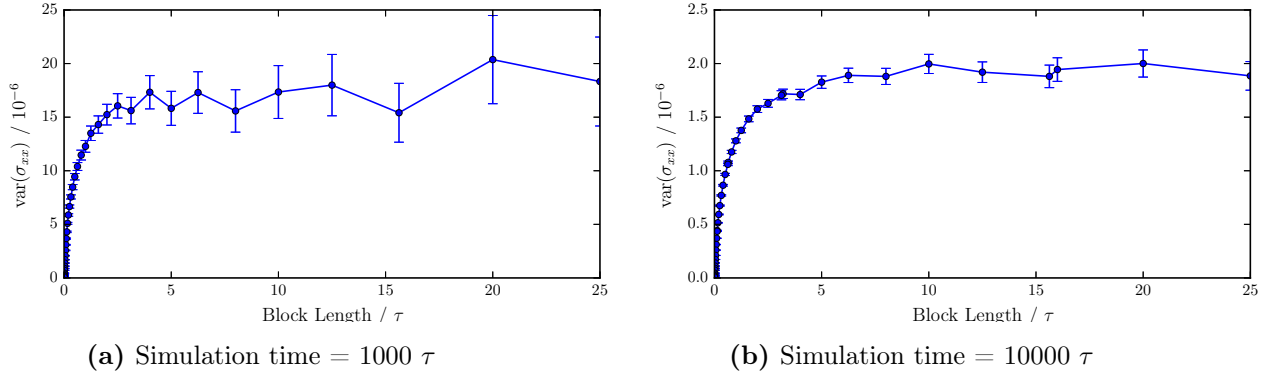


Figure 2: The blocking analysis for a system identical to those studied is compared for simulation times of 1000τ and 10000τ . Plateaus in the estimate of the variance begin at block lengths of approximately 5τ and 10τ respectively. The error in the variance does not become significant until much larger block lengths. Throughout the subsequent simulations, a block size of 10τ was used. This ensured decorrelation of the data and produced a reliable estimate of the statistical error.

A blocking-analysis for a binary-mixture identical to those used throughout this study was executed over a simulation time of $1,000 \tau$ and $10,000 \tau$, as shown in Figure 2. The plateau begins at a block length of 10τ for the long simulation and 5τ for the shorter run, with little increase in the error of the variance until a much larger block size is reached. Considering this result, a block length of 10τ was used to provide a good estimate for the error of all time-averages calculated in the subsequent simulations.

3.8 Modelling surfactant molecules

To investigate the effects of surfactants on the Marangoni effect, the surfactant molecules were modelled as a pair of Lennard-Jones particles connected by a harmonic bond with spring constant $K^* = 25$ and equilibrium bond length $r_0^* = 1.63$. Inspired by Howes and Radke’s study on non-ionic surfactants,⁴⁵ the ‘head’ particle has a stronger interaction with Fluid A particles, ($\epsilon_{H,A} = 1.33$ and $\epsilon_{H,B} = 0.17$) whilst the ‘tail’ particle has a stronger interaction with Fluid B particles ($\epsilon_{T,A} = 0.17$

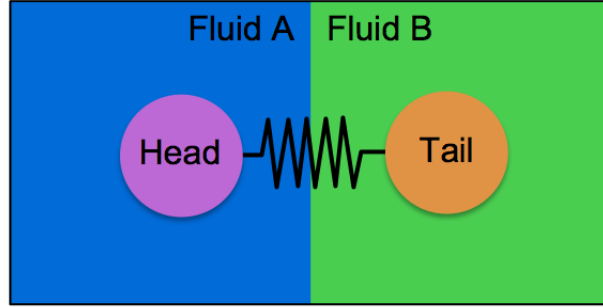


Figure 3: Surfactant molecules are represented by a pair of spherical Lennard–Jones particles connected by a harmonic bond. The head particle has a stronger interaction with Fluid A ($\epsilon_{H,A} = 1.33$ and $\epsilon_{H,B} = 0.17$) whilst the tail has a stronger interaction with Fluid B ($\epsilon_{T,A} = 0.17$ and $\epsilon_{T,B} = 1.33$). This imitates the behaviour of non-ionic surfactant molecules.

and $\epsilon_{T,B} = 1.33$). The ‘head’ and ‘tail’ groups interact with each other with strength $\epsilon_{H,T} = 1.00$.

3.9 Software details

All molecular dynamics simulations were carried out using the LAMMPS (Large Atomic and Molecular Massively Parallel Simulator) package.³³ Additional processing was carried out using Numpy.⁴⁶ All graphical figures were plotted using Matplotlib.⁴⁷

4 Results and Discussion

4.1 Binary-mixture confined between two walls

Initially, a binary-mixture of two fluids confined between two walls was studied. The fluid was prepared as described in Section 3.5 at a pressure of $P^* = 0.1$ and temperatures of $T^* = 0.8$ and $T^* = 0.9$. The confining walls were used as a piston to control the pressure.

4.1.1 Using the Virial stress

Once equilibrated, the simulations were run for 40×10^6 timesteps of length 0.001τ and the number density and Virial stress tensor were computed on every timestep. These values were then time-averaged to produce profiles for the number density and $\sigma(z')$ as shown in Figures 4 and 5.

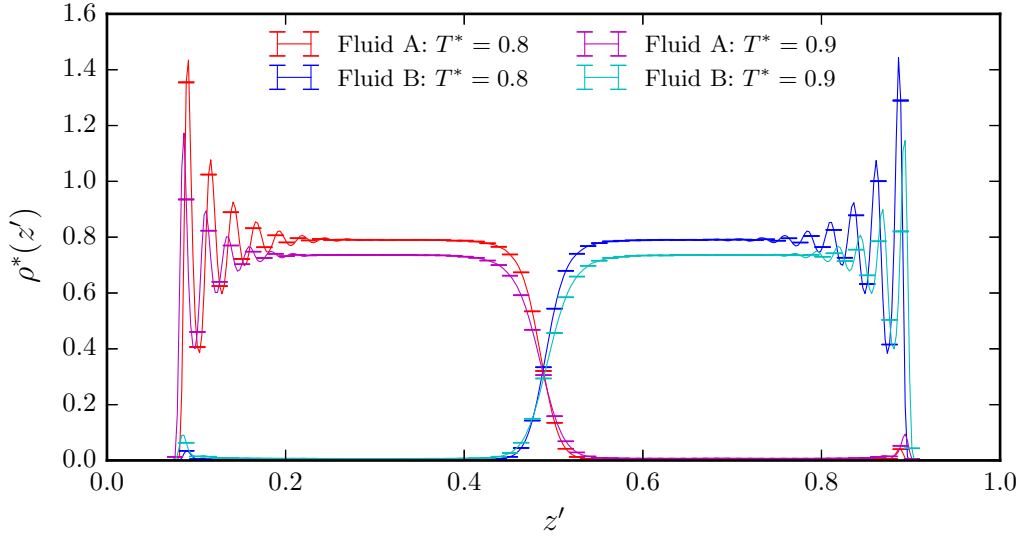


Figure 4: The number density for the two fluids confined between two walls at $T^* = 0.8$ and $T^* = 0.9$ was time-averaged over 40×10^6 timesteps of length 0.001τ . The bulk density is uniform, representing a fluid state, and the interface manifests itself as a sharp change in the densities of the two fluids. Structural layering of the fluid creates oscillations in the density close to the walls.

Both the density profile and the stress profile show the expected features of a binary-mixture. There is a uniform density in the bulk of the fluid and an interfacial region of finite width where the density of one species falls sharply and the density

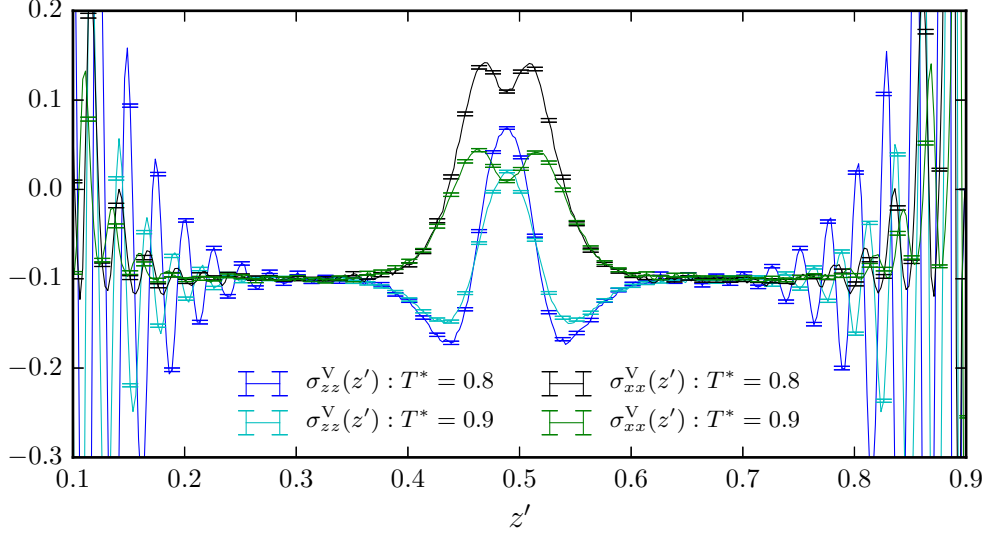


Figure 5: The Virial stress tensor components for the combined fluid confined between two walls at $T^* = 0.8$ and $T^* = 0.9$ were time-averaged over 40×10^6 timesteps of length 0.001τ . Both the normal and tangential stress show bulk values equal to $-P_{ext}$, representing the hydrostatic pressure. There is a peak in the tangential stress at the interface due to the anisotropy of the interparticle forces in this region. This can be related to the surface tension and its temperature dependence is the driving force for the Marangoni effect. There is also a change in the normal component at the interface, resulting from the dependence of the Virial stress on density deviations. Towards the wall there are temperature dependent oscillations in both components, providing the origin of the thermophoretic force.

of the other increases. Close to the walls, there are large oscillations in the density as a consequence of structural layering in the fluid close to the solid.

For the stress profile, the bulk values for the normal and tangential components are equal to $-P_{ext}$, corresponding to the hydrostatic pressure of the fluid as expected. At the interface there is a peak in the tangential stress due to the anisotropy of the intermolecular forces in this region; this can be related to the interfacial tension.⁴⁸ Furthermore, there is a change in the normal component at the interface, resulting from dependence of the Virial stress on density deviations in this region.

The time-averaged values for the stress were then used to estimate the derivative of the tangential stress with respect to temperature using Equation 15, as shown in Figure 6. This derivative shows a peak at the interface of the two fluids, providing the origin of the Marangoni force. In the bulk of the fluid the derivative is zero within statistical error, ensuring there is no force acting in this region. In addition, the derivative oscillates at the surface of the wall. This can be interpreted as a

thermophoretic force and is henceforth ignored.

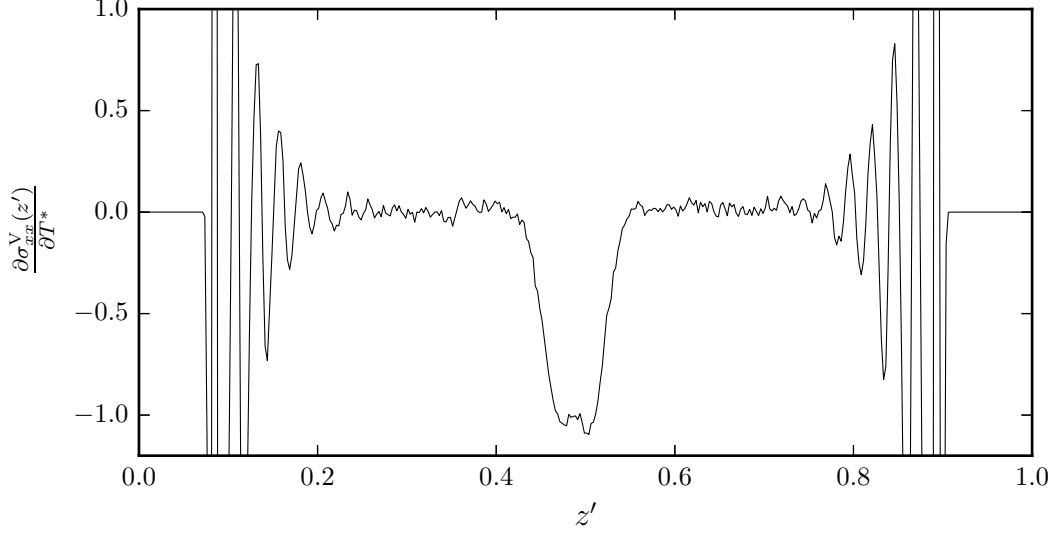


Figure 6: The derivate of the tangential component of the Virial stress with respect to temperature was calculated using the finite difference approximation. This shows a negative peak in the interfacial region. When combined with a specified temperature gradient, a force in the opposite direction to a temperature gradient is generated, imitating the Marangoni force. The oscillations at the liquid–solid surface create the thermophoretic force and are subsequently ignored.

Using the central 1/3 of the derivative profile and a temperature gradient of $\partial T^*/\partial x^* = 0.001$, an artificial Marangoni force was computed through Equation 14. This force was applied to an identical system prepared at $T^* = 0.85$. An equilibrium simulation was then run for 40×10^6 timesteps, and the time-average of the x-component of the fluid velocity $v_x^*(z')$ was computed. The momenta of the walls in the x, y plane were fixed such that they provided a stationary reference point for the fluid, creating a momentum sink.

The fluid velocity profile is shown in Figure 7. There is a sharp negative peak at the interface indicating a Marangoni flow in the opposing direction to the temperature gradient. Furthermore, the flow decays linearly away from the interface, consistent with a Couette flow arising from shear-driven fluid motion.⁴⁹

There is also a net flow in the system, suggesting an overall force acting on the fluid. The walls in the system act as a momentum sink, providing a frictional force which allows this steady-state flow to arise under the isolated effect of a temperature-gradient.

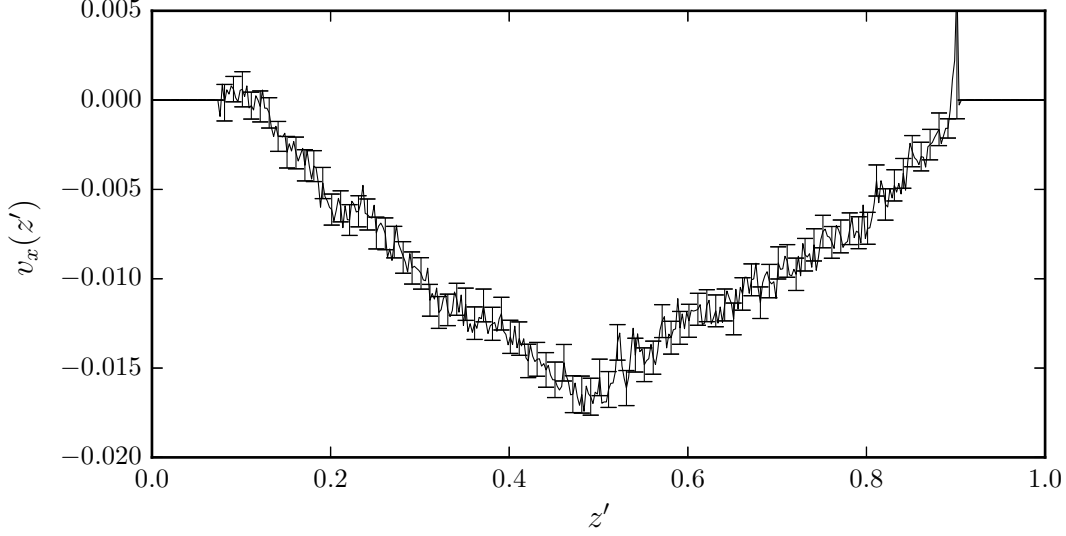


Figure 7: The velocity profile of a confined fluid at $T^* = 0.85$ with an applied force calculated from Figure 6 was time-averaged over 40×10^6 timesteps of length 0.001τ . A steady state negative interfacial peak emerges, corresponding to a Marangoni flow in the opposite direction to the temperature gradient. The magnitude of the peak velocity is approximately 0.16 and this decays linearly to zero at the surface of the bounding walls, corresponding to a Couette flow.

4.1.2 Comparing to the Irving–Kirkwood stress

Figure 5 shows the normal component of the Virial stress is not uniform across the interface. In contrast, the normal stress calculated using the Irving–Kirkwood formula does not depend on the local fluid density and should therefore be constant throughout the liquid. To verify if the difference in these methods has a significant effect on the measurement of the Marangoni force, the Irving–Kirkwood stress was also calculated.

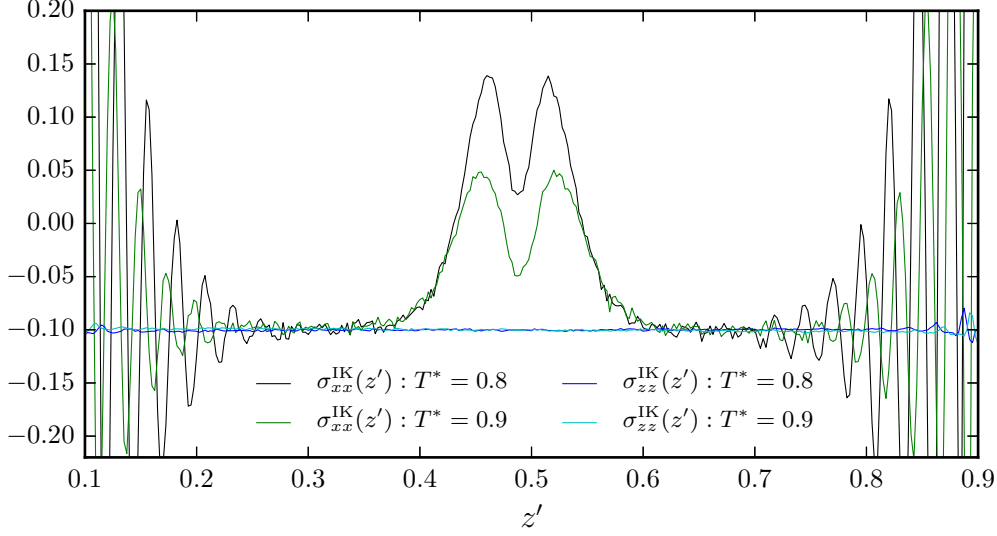


Figure 8: The Irving–Kirkwood stress tensor components for the combined fluid confined between two walls at $T^* = 0.8$ and $T^* = 0.9$ were time-averaged over 1×10^6 timesteps of length 0.001τ . Both the normal and tangential stress show bulk values equal to $-P_{ext}$, representing the hydrostatic pressure. Similar to Figure 5, there is a peak in the tangential stress at the interface due to the anisotropy of the interparticle forces in this region. However, this peak is divided into two with a reduction in the stress directly at the interface. This difference to the Virial stress arises because the Irving–Kirkwood stress does not depend on the local density. The normal components of the stress are constant across the system, as expected.

The fluids were prepared at $P^* = 0.1$ and $T^* = 0.8$ and $T^* = 0.9$ as before. Since the Irving–Kirkwood stress tensor was more computationally expensive (see Section 3.6), the equilibrium simulations were only run for 1×10^6 timesteps, resulting in a greater amount of statistical error. This produced the time-averaged stress shown in Figure 8. The tangential component shows a similar profile to the Virial stress although the interfacial peak is divided into two with a reduction in the stress directly at the interface. This difference directly at the interface arises since the Irving–Kirkwood does not depend on local density. The normal component of the Irving–Kirkwood stress is constant throughout, representing the isotropy of the system in this direction.

The finite difference method was again used to calculate the derivative of the stress with respect to temperature, and this is compared to the Virial result in Figure 9. Still focussing on the central 1/3 of the fluid, there is a good correspondence between the two derivatives and the interfacial peak occurs both across the same

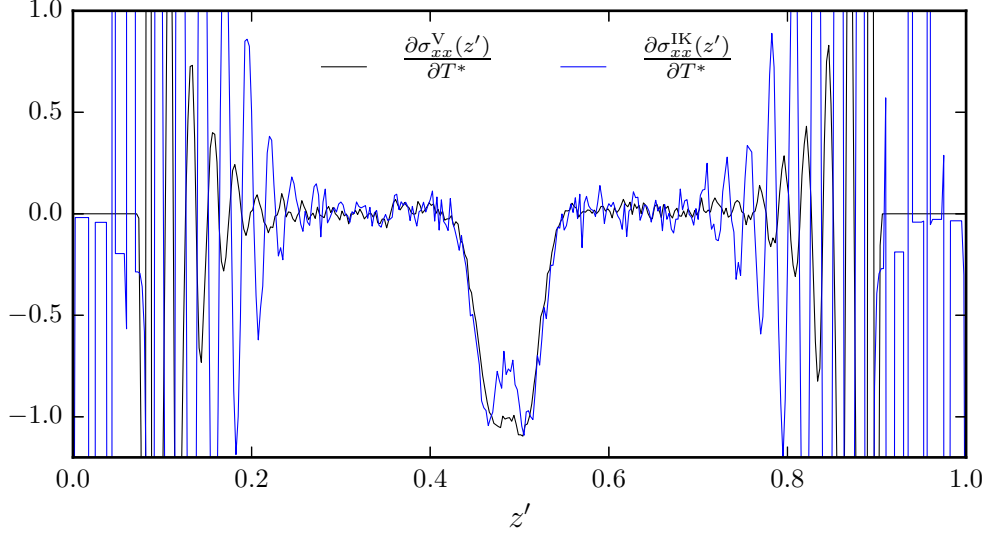


Figure 9: The derivate of the tangential component of the Irving–Kirkwood stress with respect to temperature was calculated using the finite difference approximation. There is an analogous negative peak in the interfacial region to Figure 6, with a similar magnitude and spatial extent. However, the peak in the Irving–Kirkwood derivative is split into two. This difference arises because, unlike the Virial stress, the Irving–Kirkwood stress does not depend on local density. When combined with a specified temperature gradient, a force in the opposite direction to a temperature gradient is generated, imitating the Marangoni force. The derivative in the bulk is zero, providing no body force acting on the fluid away from the interface.

spatial region and with the same maximum value. The most significant difference occurs directly at the interface, where there is a sharp reduction in the derivative of the Irving–Kirkwood stress. This is probably a result of the reduction in density at the interface affecting the Virial stress–tensor more than the Irving–Kirkwood stress–tensor.

Using a temperature gradient of $\partial T^*/\partial x^* = 0.001$ to compute the Irving–Kirkwood artificial body force, an equilibrium simulation at $T^* = 0.85$ was run for 40×10^6 timesteps. The fluid velocity was measured and compared to the result obtained using the Virial force, as shown in Figure 10. The profiles show a reasonably close correspondence, especially for the region $z' \leq 0.4$, although they deviate for higher values of z' . In particular, the flow from the Irving–Kirkwood method is not as large directly at the interface, as a result of the reduction in the force at this point. The Irving–Kirkwood velocity profile is also asymmetric despite the symmetry of the system. This asymmetry may be the result of an increase in

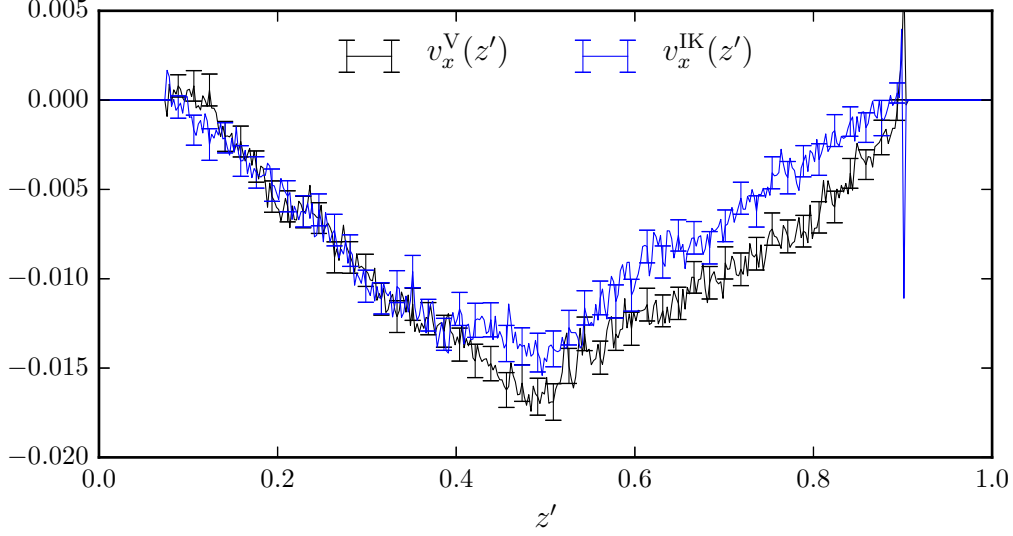


Figure 10: The velocity profile of a confined fluid at $T^* = 0.85$ with an applied force calculated from Figure 9 was time-averaged over 40×10^6 timesteps of length 0.001τ . This is compared to the velocity profile produced using the force calculated from the Virial stress. Both show a steady state negative interfacial peak, corresponding to a Marangoni flow in the opposite direction to the temperature gradient, with a linear decay into the bulk. The peak value using the force calculated from the Irving-Kirkwood stress is not as large as that using the force calculated from the Virial stress. This is a result of the reduction of the Irving-Kirkwood stress derivative directly at the interface. Moreover, the Virial flow is symmetric about the interface whilst the Irving-Kirkwood flow is not. This is probably a result of the increase in noise in the Irving-Kirkwood derivative due to a shorter simulation time.

the noise of the Irving-Kirkwood force relative to the Virial force, which results from the shorter simulation time enforced by the high computational cost of the Irving-Kirkwood analysis.

4.2 Binary-mixture periodic in 3-dimensions

Equation 1 demonstrated that the existence of a temperature gradient in the system should not be able to generate a net flow in the fluid. Levich discusses this further, describing how the interfacial flow must be accompanied by a back-flow in the bulk fluid.⁴ In the case of the binary-mixture held between two walls, the stationary walls provide a momentum sink which allows a net flow to exist within the fluid. To replicate the behaviour of an infinite fluid where a back flow may be observed, a system void of momentum sinks must be studied. For example, a binary-mixture

of two partially miscible fluids with periodic boundary conditions in all dimensions can be used.

This system, shown in Figure 1a, was prepared as described in Section 3.5 with the parameters given in Section 3.1. The distance between consecutive interfaces was $0.5L_{z^*}$. A Nosé–Hoover barostat and thermostat were used to control the pressure at $P^* = 0.1$ with temperatures of $T^* = 0.8$ and $T^* = 0.9$.

4.2.1 Comparing the Virial and Irving–Kirkwood stress

There is again an ambiguity over which stress–tensor should be used for computing the Marangoni force. Once equilibrated, the system was simulated for 10×10^6 timesteps over which the number density, Virial and Irving–Kirkwood stress were computed. As discussed before, the Irving–Kirkwood analysis was computationally expensive and this simulation length was the upper feasible limit.

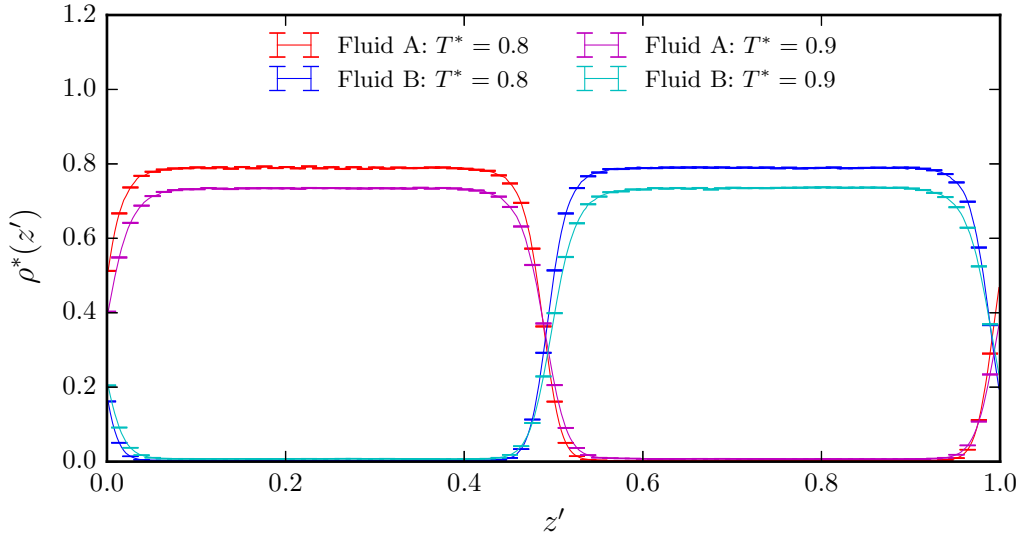


Figure 11: The number density for the two fluids periodic in all dimensions at $T^* = 0.8$ and $T^* = 0.9$ was time-averaged over 10×10^6 timesteps of length 0.001τ . The bulk density is uniform, representing a fluid state, and the interfaces manifest themselves as a sharp change in the densities of the two fluids. Between the two temperatures the position of the interface is slightly shifted, this must be corrected before calculating the stress derivative.

After this period, the density profile (plotted in Figure 11) showed a uniform density in the fluid bulk and a sharp interfacial region as expected. However, the position of the interface shifted during the simulation and was no longer coincident

for the two temperatures. Before calculating the Marangoni force from the stress profile, this shift was removed by recentering the interfaces.

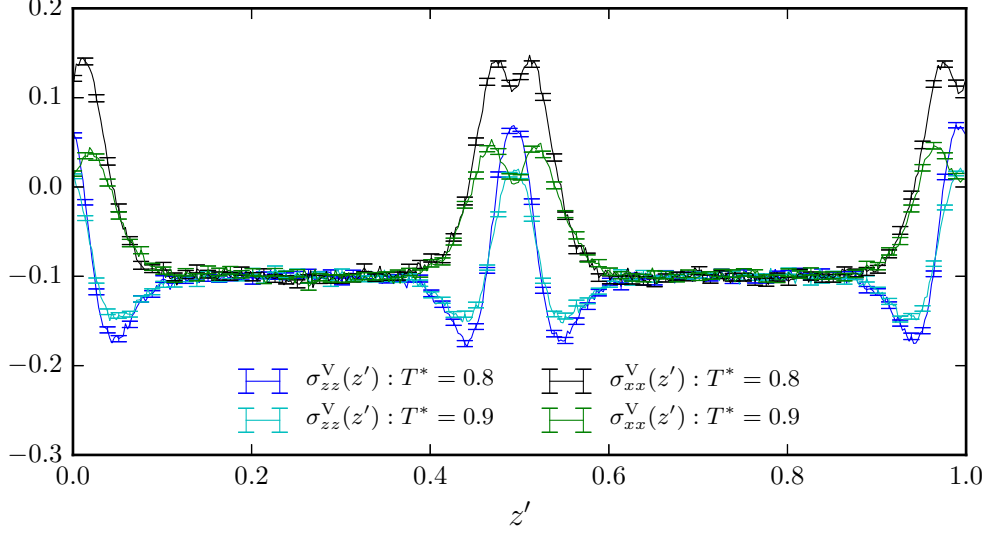


Figure 12: The Virial stress tensor components for the combined fluid periodic in all dimensions $T^* = 0.8$ and $T^* = 0.9$ were time-averaged over 10×10^6 timesteps of length 0.001τ . Both the normal and tangential stress show bulk values equal to $-P_{ext}$, representing the hydrostatic pressure. There is a peak in the tangential stress at the interface due to the anisotropy of the interparticle forces in this region. This peak has a similar form to that seen in Figure 5, and its temperature dependence provides the origin of the Marangoni effect. There is also a change in the normal component at the interface, resulting from the dependence of the Virial stress on density deviations.

The recentered Virial and Irving–Kirkwood stress profiles are plotted in Figures 12 and 13 respectively. As with the fluid confined between two walls, the bulk stress components are equal to $-P_{ext}$, corresponding to the hydrostatic fluid pressure. There is an interfacial peak in both the Virial and Irving–Kirkwood tangential stress at the interface with a similar maximum value, although the Irving–Kirkwood stress shows a stronger minimum directly at the interface. Similar to Figure 8, this is probably the result of a reduced density in the interfacial region. Furthermore, the normal component of the Irving–Kirkwood stress is clearly uniform across the interface, as expected.

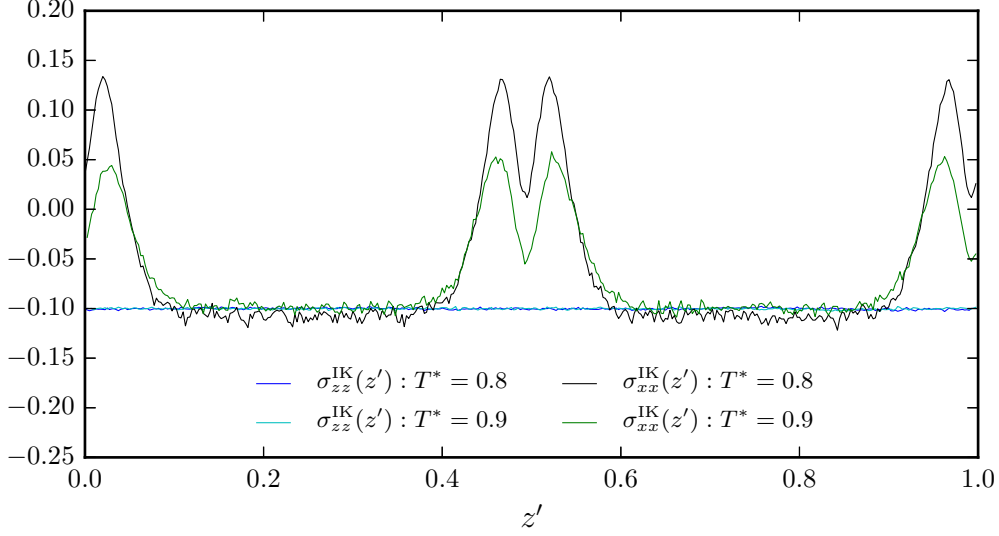


Figure 13: The Irving–Kirkwood stress tensor components for the combined fluid periodic in all dimensions $T^* = 0.8$ and $T^* = 0.9$ were time-averaged over 10×10^6 timesteps of length 0.001τ . Both the normal and tangential stress show bulk values equal to $-P_{ext}$, representing the hydrostatic pressure. There is a peak in the tangential stress at the interface due to the anisotropy of the interparticle forces in this region. This peak has a similar form to that seen in the Virial stress, although they deviate directly at the interface. Since the Irving–Kirkwood stress does not depend on local density, the normal component is uniform across the system, as expected.

Using these stress profiles, the derivative of the stress with respect to temperature was calculated through the finite difference approach. The derivative profile was adjusted by subtracting the average from each value, ensuring the integral over all space was zero, as shown in Figure 14. This guaranteed there would be no net applied force acting on the fluid, even in the absence of a momentum sink in the system.

The derivative profile shows a similar interfacial peak to Figure 9. The maximum values are similar, suggesting that fixing the total force to zero correctly adjusts the derivatives to give a physically meaningful Marangoni force. Again, there is a reasonably good correspondence between the derivatives calculated from the Irving–Kirkwood and Virial stress tensors, and the magnitude of the Irving–Kirkwood peak is reduced directly at the interface. In the bulk fluid, the derivative opposes the interfacial peak, generating the back force which balances the Marangoni force. However, the profile as a whole shows too much noise for the fine-structure to be determined and is not of sufficient quality to be used in calculating an artificial

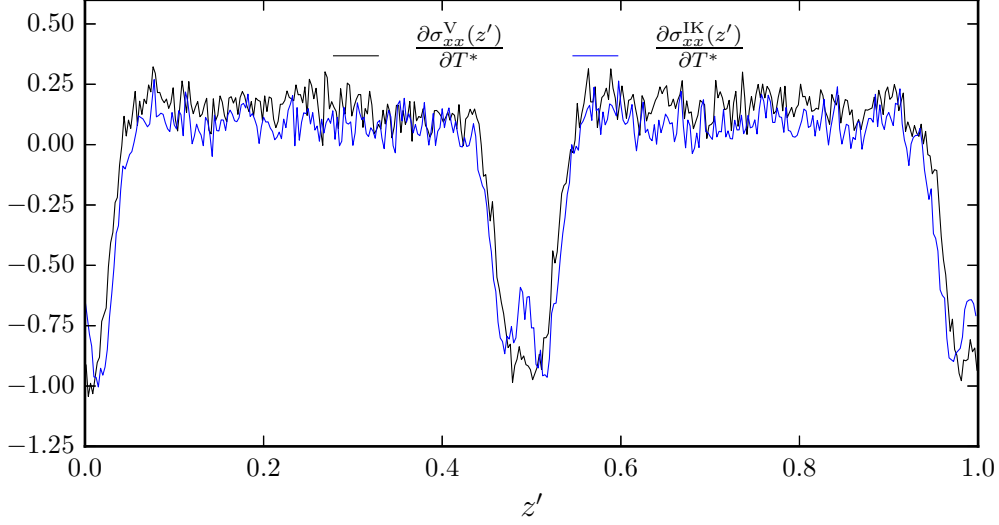


Figure 14: The derivate of the tangential component of the Irving–Kirkwood and Virial stress with respect to temperature was calculated using the finite difference approximation. The average value was subtracted to ensure the integral of the derivative profile over all space was zero. Both the Virial and Irving–Kirkwood stress derivatives show a negative peak at the interface, with a similar maximum value and spatial extent. However, there is too much noise in these profiles, obscuring the fine structure and preventing a definitive comparison. Furthermore, these derivatives are not precise enough to be useful for calculating an artificial body force.

body–force.

4.2.2 Reducing the noise in the force–profile

To generate a profile with a sufficiently low noise requires either a larger system size or a longer simulation time. Both of these increase the computational cost of calculating the Irving–Kirkwood stress beyond a practical level, and instead the Virial stress must be used. Considering how similar the Virial and Irving–Kirkwood derivative profiles appear in Figure 9, using the Virial stress does not create too much deviation from the more suitable Irving–Kirkwood stress, whilst enabling a much longer simulation time.

The reduced noise stress was calculated by running the equilibrium systems for 30×10^6 timesteps. Recentering the interfaces generated the Virial stress profile shown in Figure 15. For both temperatures, the profiles show much less noise compared to Figure 12, especially in the bulk region, and the interfacial peaks are more symmetric.

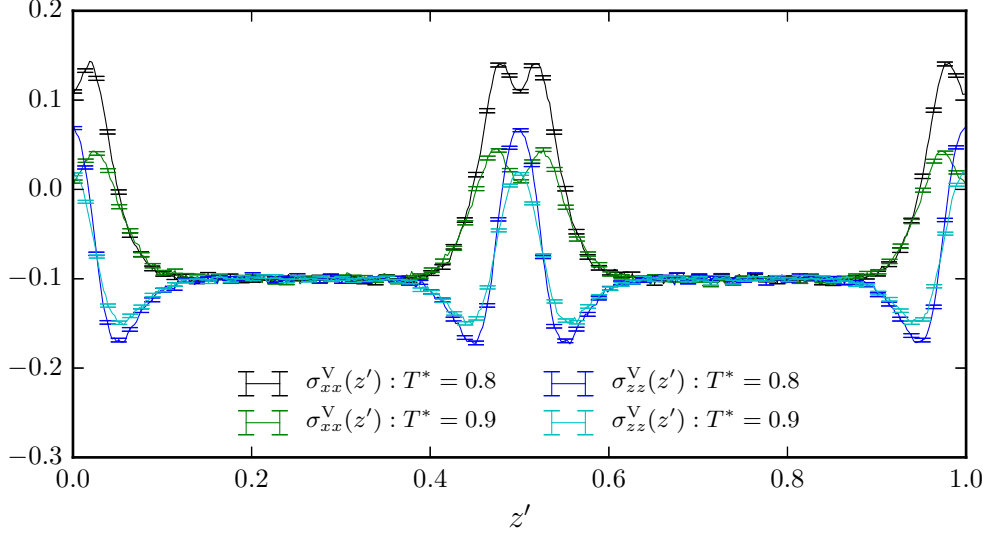


Figure 15: The Virial stress tensor components for the combined fluid periodic in all dimensions $T^* = 0.8$ and $T^* = 0.9$ were time-averaged over 30×10^6 timesteps of length 0.001τ . This produced a significant reduction in noise relative to Figure 12. As before, both the normal and tangential stress show bulk values equal to $-P_{ext}$, representing the hydrostatic pressure. There is a peak in the tangential stress at the interface due to the anisotropy of the interparticle forces in this region. The normal component at the interface also deviates from the bulk value as a result of the dependence of the Virial stress on the local density.

Using these stress profiles, the derivative of the stress-tensor with respect to temperature was again computed using the finite difference and the average value subtracted to give the profile shown in Figure 16. There is a dramatic reduction in the noise compared to Figure 14, with a sharp peak at the interface and an opposing stress derivative in the bulk regions.

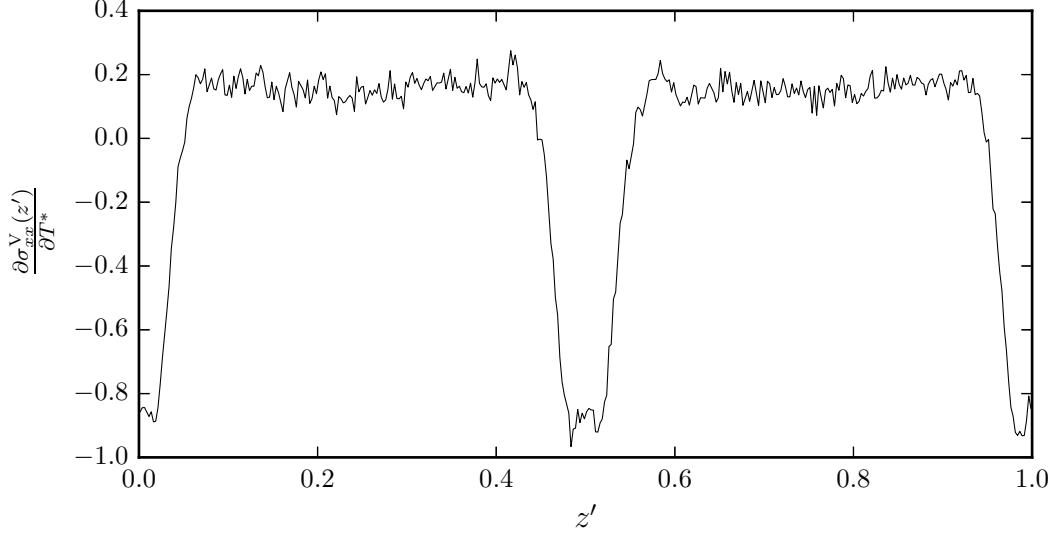


Figure 16: The derivate of the tangential component of the Virial stress was calculated using the finite difference approach. The average value was subtracted to ensure the integral of the derivative profile over all space was zero. There is a significant reduction in noise compared to Figure 14. A sharp, negative peak can be seen at the interface, leading to the Marangoni force, and an opposing derivate occurs in the bulk of the fluid, yielding a balancing back flow.

Using the stress derivative given in Figure 16 and a temperature gradient of $\partial T^*/\partial x^* = 0.001$, an artificial body force was computed. The body force was recentered to ensure the Marangoni peak was aligned with the interfacial region, and this was applied in an equilibrium simulation at $T^* = 0.85$. This simulation was run for 40×10^6 timesteps, and $v_x^*(z')$ was computed to give the flow velocity plotted in Figure 17.

Despite the simulation being run for a long timescale, the velocity profile still retains a lot of statistical noise. It would be difficult practically to reduce this noise further. Moreover, the average velocity (indicated by the hashed line) is non-zero, indicating centre-of-mass motion during the simulation. This motion occurs even though the stress derivative has been adjusted to give no net force overall. It is likely that in the absence of a momentum sink for a system like this, it would be very difficult to completely remove this net flow without artificially fixing the centre-of-mass throughout the simulation.

Despite this, the relative motion across the fluid can still be considered, and there does appear to be a velocity peak at the interface (with $v < v_{\text{COM}}$), corresponding to a Marangoni flow, with a back flow in the bulk fluid (with $v > v_{\text{COM}}$) as predicted.

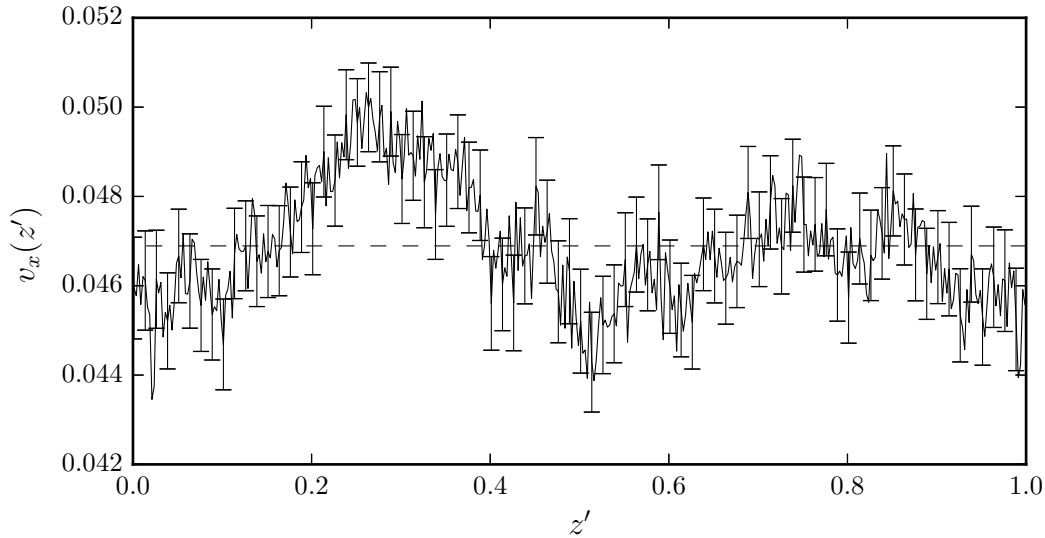


Figure 17: The velocity profile of an infinite binary-mixture at $T^* = 0.85$, with an applied force calculated using Figure 16 and temperature gradient of $\partial T^*/\partial x^* = 0.001$, was time-averaged over 40×10^6 timesteps of length 0.001τ . A non-equilibrium emerges with a non-zero average velocity (indicated by the hashed line), despite the average derivative being fixed to zero. It is unlikely this could be removed without artificially fixing the centre-of-mass. Despite this, the fluid velocity relative to this centre-of-mass motion suggests a Marangoni flow at the interfaces with an opposing flow in the bulk regions, as predicted by Levich.⁴

This result is, however, somewhat ambiguous and there was insufficient time to improve this simulation further.

4.3 The effect of surfactants

Surfactant molecules decrease the surface free energy of interfaces, as they have a favourable interaction with both fluids and bridge the interfacial plane. This reduction in surface tension should also cause a decrease in the surface tension gradient and thus the Marangoni effect, as observed experimentally.^{22–25}

To model this, the non-ionic surfactant molecules described in Section 3.8 were added to the binary-mixture confined between two walls. This system was chosen since the results of Section 4.1 showed it allowed a steady state flow to be generated and modelled effectively.

The surfactant molecules were added to a single plane between the two fluids in the initial lattice before melting. A certain fraction of these molecules were then removed to vary the surfactant concentration, quantified as a fraction of the total

number of fluid particles present,

$$\text{Surfactant Fraction} \equiv \frac{N_{\text{surfactant}}}{N_{\text{surfactant}} + N_{\text{fluid}}}. \quad (32)$$

This allowed the surfactant fraction to be varied between 0 and 0.0323.

Taking fractions of 0.000, 0.0031, 0.0098, 0.0194, 0.0264, 0.0298 and 0.0323, the fluid was prepared as described in Section 3.5, with a pressure of $P^* = 0.1$ and temperatures of $T^* = 0.8$ and $T^* = 0.9$. A piston barostat and Nosé–Hoover thermostat were used and each system was run at equilibrium for 30×10^6 timesteps of length 0.001τ .

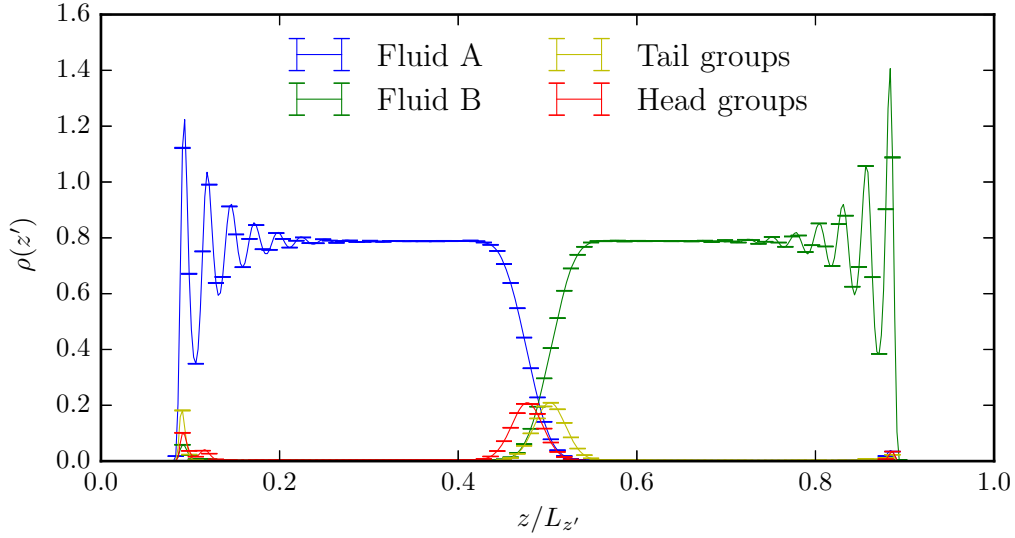


Figure 18: The number density for the confined binary-mixture with a non-ionic surfactant fraction of 0.0194, pressure of $P^* = 0.1$ and at $T^* = 0.8$ was time-averaged over 30×10^6 timesteps of length 0.001τ . There is a uniform density in the bulk, and an interface represented by a sharp change in the densities of Fluid A and Fluid B. The surfactant particles are localised at the interface with a low solubility. They show the correct orientation, with ‘Head’ particles interacting most strongly with Fluid A and ‘Tail’ particles with Fluid B.

The resulting number density of each species shows a uniform bulk density, a sharp interface and peaks for the head and tail groups located at the interface, as shown for $T^* = 0.8$ and a surfactant fraction of 0.0194 in Figure 18. The surfactant molecules were correctly oriented with head groups interacting with Fluid A and tail groups with Fluid B.

The Virial stress was computed during the equilibrium simulations and used to compute the derivative of the stress with respect to temperature for each surfactant

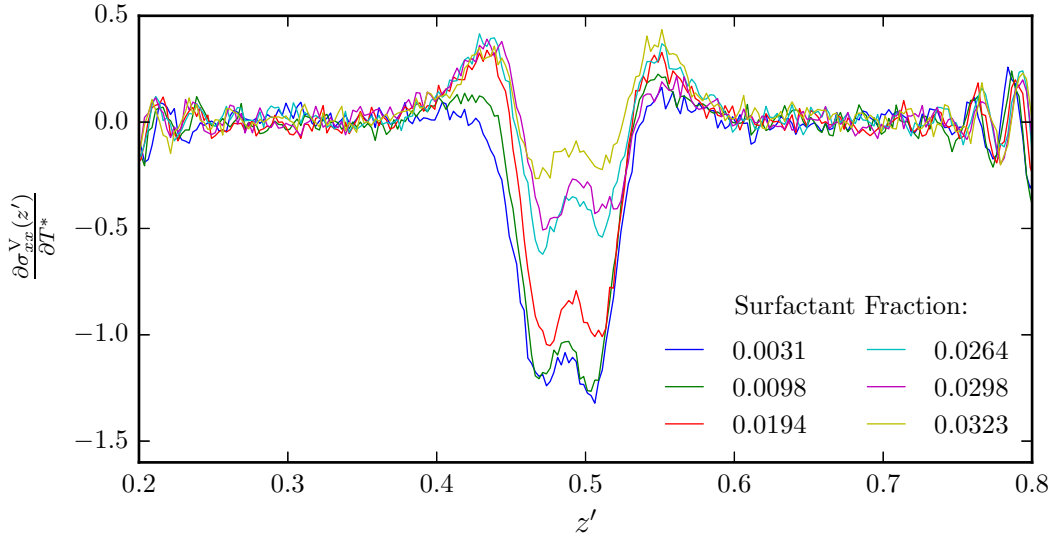


Figure 19: The derivative of the tangential component of the Virial stress with respect to temperature was calculated for a range of surfactant fractions using the finite difference approximation. For a low surfactant fraction, there is strong interfacial peak providing the origin of the Marangoni force. As the amount of surfactant is increased, the strength of this peak decreases to zero indicating the eradication of the Marangoni effect. Two smaller positive peaks on either side of the centre also develop for higher surfactant fractions. This probably results from an increase in the number density in this region, due to localisation of the surfactant particles at the interface.

fraction. These results, plotted in Figure 19, show a pronounced reduction in the magnitude of the interfacial peak as the surfactant fraction increases, corresponding to the expected reduction in the Marangoni force.

Two smaller positive peaks on either side of the centre also develop for higher surfactant fractions. It is unclear exactly what these peaks correspond to. They may simply be the result of an increase in the fluid density, due to localisation of the surfactant particles in this region and the dependence of the Virial stress on local density. An increase in surfactant fraction would then exaggerate this density change. In future, this could be verified by computing the Irving–Kirkwood stress, where any peaks due to density deviations should disappear.

Furthermore, the harmonic forces in the surfactant molecules may provide a contribution to these peaks in the stress. The physical significance of this contribution could be investigated by varying the spring constant for the surfactant bond and noting any changes in the magnitude of these secondary peaks.

Using a temperature gradient of $\partial T^*/\partial x^* = 0.001$, the central 1/3 of the stress

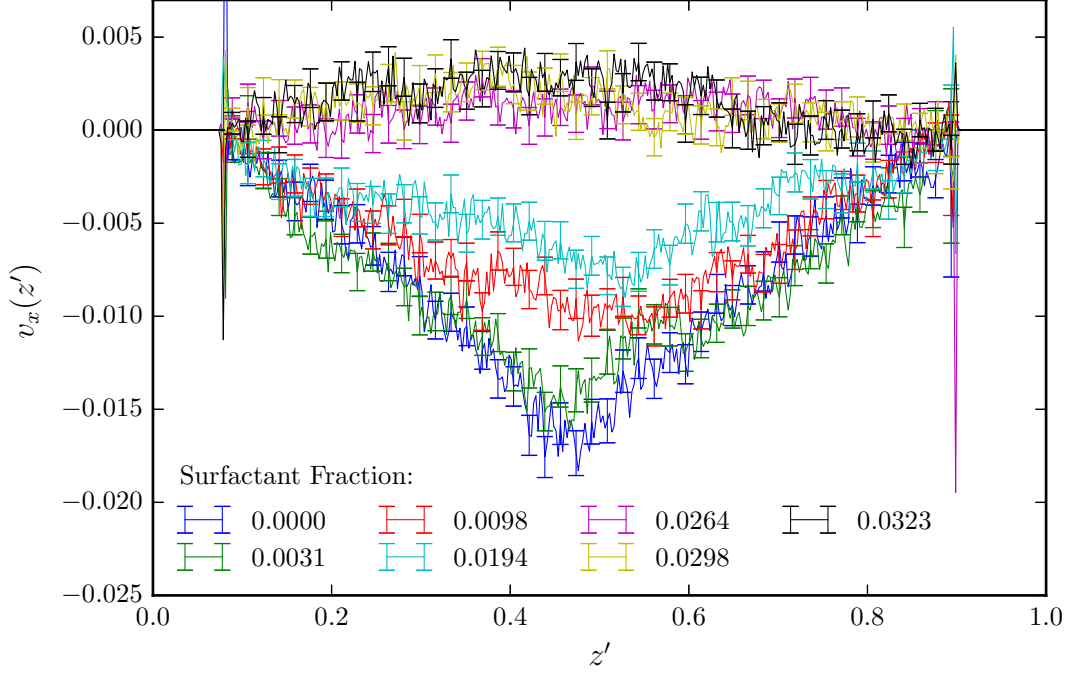


Figure 20: The velocity profile of an confined binary-mixture at $T^* = 0.85$, with an applied force calculated using Figure 19 and temperature gradient of $\partial T^*/\partial x^* = 0.001$, was time-averaged over 40×10^6 timesteps of length 0.001τ for a range of surfactant fractions. For a low surfactant fraction, the flow profile closely resembles that of the non-surfactant system (Figure 7, with a negative interfacial peak and a linear decay into the bulk. As the amount of surfactant increases there is a reduction in the magnitude of this peak until the Marangoni flow essentially disappears. Moreover, the peak becomes less sharp at higher surfactant fractions. This is probably due to the non-uniform viscosity created by the added surfactant molecules.

derivative profiles in Figure 19 were used to compute an artificial body force, which was applied to simulations at $T^* = 0.85$. These were run for 30×10^6 timesteps over which $v_x(z')$ was measured and plotted in Figure 20. There is a clear decrease in the interfacial velocity as the surfactant fraction is increased, suggesting a retardation of the Marangoni effect induced by the surfactant molecules.

The interfacial velocity can be taken as the peak of the flow shown in Figure 20. Comparing these values against the surfactant fraction shows a reduction in the magnitude of this peak value as the surfactant fraction increases, as shown in Figure 21. Above a fraction of 0.025 it appears the Marangoni effect has been removed completely. This retardation has been observed experimentally by Barton

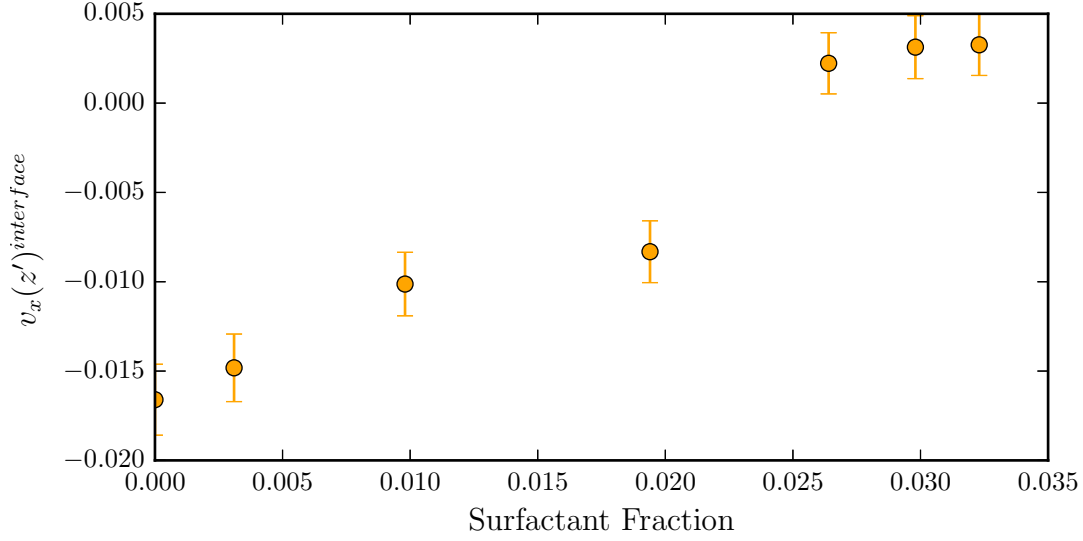


Figure 21: Comparing the surfactant fraction to the interfacial velocity demonstrates the retardation of the Marangoni flow in the presence of surfactant molecules. Above a fraction of 0.025, this velocity is essentially zero, although there is small velocity in the opposite direction to the Marangoni flow. This may be the result of the secondary peaks that emerge in Figure 19 which only become significant for high surfactant fractions.

and Subramanian, and is discussed in their study on the relation between droplet size and upward motion under a vertical temperature gradient.²⁴ They note that droplets actually sink on the addition of a nonionic surfactant, indicating the eradication of the Marangoni force and the dominance of gravity.

The sharpness of the Marangoni flow peak in Figure 20 also decreases as the surfactant fraction increases and no longer fits the Couette model as conclusively. This may be a result of the reduction in viscosity at the interface due to the presence of surfactant molecules, giving a non-uniform viscosity across the fluid. To confirm this, the viscosity could be measured using the Green–Kubo relation,

$$\eta = \frac{1}{Vk_{\text{B}}T} \int_0^\infty \langle \sigma_{xy}(\tau) \sigma_{xy}(0) \rangle d\tau, \quad (33)$$

providing a good basis for future work in this area.

5 Concluding Remarks

Using equilibrium simulations at two close temperatures, the derivative of the tangential component of the stress tensor with respect to temperature was estimated for binary-mixtures through a finite-difference method. The derivatives of the Virial and Irving-Kirkwood stresses were calculated for a mixture confined between two walls, and in both cases there was a similar negative interfacial peak. Combining with a temperature gradient, an artificial body force was computed and applied in a third equilibrium simulation, resulting in a non-equilibrium with a net interfacial flow. This was interpreted as a Marangoni flow and occurred in the opposite direction to the applied temperature gradient, as expected. The confining walls provided a momentum sink in the system, exerting a frictional force on the fluid and allowing a steady state flow to be achieved.

The same method was then applied for a binary-mixture periodic in all dimensions, and a similar peak in the stress derivative was observed. However, the fine structure of this derivative was obscured by significant noise. This was reduced by running the simulation for a longer time period. As a result, only the Virial stress was feasible for calculating a sufficiently precise gradient profile.

In the absence of a momentum sink, the stress derivative was adjusted to ensure no net force was applied on the system, and was used to calculate an artificial body force. Applying this force produced a flow profile showing a negative peak at the interfaces relative to a net centre-of-mass motion, and an associated back flow in the bulk of the fluid.

The origin of the centre-of-mass motion is unclear. It is possible, although unlikely, that this is the result of errors induced by noise in the applied force. For example, errors in the average derivative will cause the derivative profile to be incorrectly recentred, and a net applied force could result. Running the initial equilibrium simulations for an even longer period could allow a more precise force to be calculated and the effect of noise verified.

Alternatively, the centre-of-mass could be artificially held stationary throughout the simulation. However, this would be rather unphysical, since observing a stationary centre-of-mass is essential to verifying the correct behaviour of Marangoni flows. Fixing the centre-of-mass would allow only the relative motion of different fluid regions to be observed.

Having established a working system in the form of the fluid confined between two walls, the effect of surfactants on Marangoni flows was investigated by adding

different concentrations of non-ionic surfactant molecules into the interfacial region. The tangential Virial stress was again computed at two temperatures and its derivative with respect to temperature was estimated through the finite difference. As the concentration of surfactant increased, there was a reduction in the magnitude of the negative interfacial peak and the emergence of two secondary positive peaks on either side of the interface..

The stress derivatives were used to calculate an artificial body force that was then applied in a third equilibrium simulation. The magnitude of the resulting Marangoni flow was seen to decrease to zero as the surfactant concentration increased, in agreement with experimental studies. Furthermore, the shape of the velocity profile deviated from the linear decay observed in the absence of surfactant. This may be due to a non-uniform fluid viscosity, since the addition of surfactants should decrease the viscosity of the interfacial region.

5.1 Future directions of study

There are a number of ambiguities in the results reported which may be verified through further study. For example, if more time was available it would be interesting to compute more accurate force profiles from the Irving–Kirkwood stress by using a larger system. This could be made more efficient by implementing the Irving–Kirkwood analysis in parallel.

Furthermore, by introducing a contribution from the harmonic bonding into this analysis, it could be used to study systems with added surfactant. Using the Irving–Kirkwood stress would confirm whether the secondary peaks observed as surfactant fraction increases are the result of an increase in local density due to the presence of surfactant particles, or some other significant physical feature.

It would also be interesting to compute the viscosity across the liquid and compare this for the pure fluid and the fluid with surfactant present. As described in Section 4.3, this can be calculated using a Green–Kubo relation. Comparing the shape of the flow profile to the uniformity in the viscosity would allow the deviation from the Couette flow model to be investigated.

Beyond this, linear response theory suggests that the flow induced by a temperature gradient could be computed as:

$$\langle v_x \rangle = \frac{\nabla T}{T} V \int_{\tau=0}^{\infty} \langle J_x(0) Q_x(\tau) \rangle d\tau, \quad (34)$$

where J and Q are the mass and heat flux respectively. By computing this average velocity for the mixture confined between two walls, both with and without an applied body force, Equation 34 could allow a general relation between flow velocity and temperature gradient to be developed. This could be compared for the bulk and interfacial regions, since there should be no correlation between the heat flux and mass flux away from the interfaces.

In addition to this, a greater understanding could be developed using Onsager's reciprocal rule, as employed by Derjaguin et al. This could be achieved by applying a pressure gradient to a simulation and measuring the resulting heat flux. From the relation of these quantities, the mass flux from a temperature gradient could be computed.

Finally, once informative methods for the basic study of Marangoni flows have been developed, the natural progression would be to investigate different systems and geometries. For example, it would be interesting to study a non-symmetric binary-mixture or to replicate the thermophoresis of bubbles and drops under a temperature gradient, as observed experimentally.

Through the results of this study, combined with future work, a greater understanding of the relationship between the stresses within a fluid and the velocity due to a temperature gradient can be achieved. Ultimately this is working towards a microscopic description and a more comprehensive understanding of the Marangoni effect.

References

1. J. THOMPSON, *Phil. Mag.* **10**, 330 (1855).
2. C. MARANGONI, *Ann. der Phys* **22**, 337 (1871).
3. B. V. DERJAGUIN, N. V. CHURAEV, and V. M. MULLER, *Surface Forces*, Consultants Bureau, 1987.
4. V. G. LEVICH, *Physiochemical Hydrodynamics*, Prentice–Hall, 1962.
5. J. L. ANDERSON, *Ann. Rev. Fluid Mech.* **21**, 61 (1989).
6. R. CINI, G. LOGLIO, and A. FICALBI, *J. Colloid Interface Sci.* **41**, 287 (1972).
7. W. V. KAYSER, *J. Colloid Interface Sci.* **56**, 622 (1975).
8. H. A. MAIER, P. A. BOPP, and M. J. HAMPE, *Can. J. Chem. Eng.* **90**, 833 (2012).
9. D. C. VENERUS and D. N. SIMAVILLA, *Scientific Reports* **5**, 16162 (2015).
10. R. TADMOR, *J. Colloid Interface Sci.* **332**, 451 (2009).
11. R. VUILLEUMIER, V. EGO, L. NELTNER, and A. M. CAZABAT, *Langmuir* **11**, 4117 (1995).
12. F. GIRARD, M. ANTONI, and K. SEFIANE, *Langmuir* **24**, 9207 (2008).
13. H. HU and R. G. LARSON, *J. Phys. Chem. B* **110**, 7090 (2006).
14. K. SEFIANE, *Adv. Colloid Interface Sci.* **206**, 372 (2014).
15. C. V. STERNLING and L. E. SCRIVEN, *AIChE J.* **5**, 514 (1959).
16. A. D'AUBETERRE, R. DA SILVA, and M. E. AGUILERA, *Int. J. Heat Mass Transf.* **32**, 677 (2005).
17. P. LYFORD, H. PRATT, F. GREISER, and D. SHALLCROSS, *Can. J. Chem. Eng.* **76**, 167 (1998a).
18. P. LYFORD, H. PRATT, F. GREISER, and D. SHALLCROSS, *Can. J. Chem. Eng.* **76**, 175 (1998b).

-
19. R. S. SUBRAMANIAN and R. BALASUBRAMANIAN, *The motion of bubbles and drops in reduced gravity*, Cambridge University Press, 2001.
 20. N. O. YOUNG, J. S. GOLDSTEIN, and M. J. BLOCK, *J. Fluid Mech.* **6**, 350 (1959).
 21. S. C. HARDY, *J. Colloid Interface Sci.* **69**, 157 (1979).
 22. H. H. KIM and R. S. SUBRAMANIAN, *J. Colloid Interface Sci.* **127**, 417 (1989a).
 23. H. H. KIM and R. S. SUBRAMANIAN, *J. Colloid Interface Sci.* **130**, 112 (1989b).
 24. K. D. BARTON and R. S. SUBRAMANIAN, *J. Colloid Interface Sci.* **133**, 211 (1990).
 25. J. CHEN and K. J. STEBE, *J. Fluid Mech.* **340**, 35 (1997).
 26. J.-P. HANSEN and I. R. MCDONALD, *Theory of Simple Liquids*, Academic Press, 4 edition, 2013.
 27. F. VARNIK, J. BACHNAGEL, and K. BINDER, *J. Chem. Phys.* **113**, 4444 (2000).
 28. R. CLAUSIUS, *Phil. Mag.* **40**, 122 (1870), Engl. Trans.
 29. J. S. ROWLINSON and B. WIDOM, *Molecular Theory of Capillarity*, Clarendon Press, 1982.
 30. J. P. R. B. WALTON, D. J. TILDESLEY, J. S. ROWLINSON, and J. R. HENDERSON, *Mol. Phys.* **48**, 1357 (1983).
 31. J. G. KIRKWOOD and F. P. BUFF, *J. Chem. Phys.* **17**, 338 (1949).
 32. J. H. IRVING and J. G. KIRKWOOD, *J. Chem. Phys.* **18**, 817 (1950).
 33. S. PLIMPTON, *J. Comp. Phys* **117**, 1 (1995).
 34. E. DIAZ-HERRERA, G. RAMIREZ-SANTIAGO, and J. A. MORENO-RAZO, *J. Chem. Phys.* **123**, 184507 (2005).
 35. F. J. MARTÍNEZ-RUIZ, A. I. MORENO-VENTAS BRAVO, and F. J. BLAS, *J. Chem. Phys.* **143**, 104706 (2015).

-
36. D. FRENKEL and B. SMIT, *Understanding Molecular Simulation*, Academic Press, 2 edition, 1996.
 37. SCHNEIDER and STOLL, *Phys. Rev. B* **17**, 1302.
 38. H. C. ANDERSON, *J. Chem. Phys.* **72**, 2384 (1980).
 39. S. NOSÉ, *Mol. Phys.* **52**, 255 (1984).
 40. S. NOSÉ, *J. Chem. Phys.* **81**, 511 (1984).
 41. W. HOOVER, *Phys. Rev. A* **31**, 1695 (1985).
 42. B. SMIT, *J. Chem. Phys.* **96**, 8639 (1992).
 43. P. A. BOPP, J. B. BUHN, H. A. MAIER, and M. J. HAMPE, *Chem. Eng. Comm.* **195**, 1437 (2008).
 44. H. FLYVBJERG and H. PETERSEN, *J. Chem. Phys.* **91**, 461 (1989).
 45. A. J. HOWES and C. J. RADKE, *Langmuir* **23**, 1835 (2007).
 46. S. VAN DER WALT, S. C. COLBERT, and G. VAROQUAUX, *Comput. Sci. Eng.* **13**, 22 (2011).
 47. J. D. HUNTER, *Comput. Sci. Eng.* **9**, 90 (2007).
 48. A. MARCHAND, J. H. WEIJS, J. H. SNOEIJER, and B. ANDREOTTI, *Am. J. Phys.* **79**, 999 (2011).
 49. B. S. MASSEY, *Mechanics of Fluids*, CRC Press, 9 edition, 2012, Revised by J. Ward-Smith.